Efficient parametric frequency conversion in lithium niobate nanophotonic chips

JIA-YANG CHEN,[1,2] YONG MENG SUA,[1,2] ZHAO-HUI MA,[1,2] CHAO TANG,[1,2] ZHAN LI,[1,2] AND YU-PING HUANG[1,2,*]

[1]*Department of Physics and Engineering Physics, Stevens Institute of Technology, 1 Castle Point Terrace, Hoboken, New Jersey 07030, USA*
[2]*Center for Quantum Science and Engineering, Stevens Institute of Technology, 1 Castle Point Terrace, Hoboken, New Jersey 07030, USA*
*yhuang5@stevens.edu

Abstract: Chip-integrated nonlinear photonics holds the key for advanced optical information processing with superior performance and novel functionalities. Here, we present an optimally mode-matched, periodically poled lithium niobate nanowaveguide for efficient parametric frequency conversions on chip. Using a 4-mm nanowaveguide with subwavelength mode confinement, we demonstrate second harmonic generation with efficiency over 2200% $W^{-1}cm^{-2}$, and broadband difference frequency generation over a 4.3-THz spectral span. These allow us to generate correlated photon pairs over multiple frequency channels via spontaneous parametric down conversion, all in their fundamental spatial modes, with a coincidence to accidental ratio as high as 600. The high efficiency and dense integrability of the present chip devices may pave a viable route to scalable nonlinear applications in both classical and quantum domains.

1. Introduction

Second order optical nonlinearities ($\chi^{(2)}$) are central to a plethora of classical and quantum optics studies and applications. In particular, optical parametric processes such as second harmonic generation (SHG), quantum frequency conversion, and parametric down conversion are quintessence for many quantum photonics techniques in computing [1], communications [2,3], and metrology [4]. Over the years, lithium niobate (LN) has been a preferred material of choice for those applications due to its large $\chi^{(2)}$ tensor ($d_{33} \sim$27 pm/V), ultrafast electro-optic responses, and a low-loss optical window across from 0.35 μm to 5.2 μm. Yet typical lithium niobate devices take the forms of bulk crystal or weakly confined waveguides [5], which are challenging for dense integration, as needed for hosting complex functionalities. Furthermore, the weak mode confinement limits the achievable interaction and thus requires high laser power to obtain strong nonlinear effects. Although there has been some attempts on heterogeneous lithium niobate on silicon [6,7] or silicon nitride [8] platform, their nonlinear conversion efficiency is limited due to imperfect poling quality or lateral leakage [9].

Quite recently, the advent of monolithic LN integrated photonics with high index contrast and low loss points to integrated nonlinear devices on chip [10]. With strong field enhancement by subwavelength mode confinement, they promise to overcome the aforementioned deficiencies, leading to efficient devices with much enhanced nonlinear interaction strength, smaller footprints, and highly scalable [11]. However, the phase matching requirement for efficient nonlinear processes is stringent in LN nanostructures, which hinders the development of integrated nonlinear photonic chips. Several approaches have been put forward to achieve phase matching, including by utilizing birefringent and geometric dispersion [12,13] or higher-order mode interactions [14,15]. Nonetheless, both approaches are fundamentally limited, where the former cannot access the d_{33} tensor with the highest $\chi^{(2)}$ susceptibility, while latter suffers the poor mode overlapping between the fundamental and higher-order modes. In contrast, by periodically

inverting the optical crystal domains, quasi phase matching can be achieved among fundamental spatial modes while taking advantage of the d_{33} tensor element, both crucial for strong nonlinear interactions. In addition, this facilitates the interfacing of LN chips with other devices, such as quantum emitters [16,17] and optical fibers, thereby allowing interconnection and reconciliation of quantum resources on disparate platforms towards practical deployment of scalable quantum network [18–20].

In this paper, we design and fabricate periodically poled lithium niobate (PPLN) nanowaveguides with carefully tailored quasi-traverse-electric (TE$_{00}$) mode profile and achieving sub-wavelength light confinement for efficient parametric frequency conversions. This allows us to harness the highest $\chi^{(2)}$ nonlinear susceptibilities while benefiting from maximum modes overlap of interacting wavelengths and strong light confinement. We observe high conversion efficiency of 2200% $W^{-1}cm^{-2}$, which is comparable to the record efficiency demonstrated on PPLN nanowaveguide of similar length [11]. Furthermore, we demonstrate difference frequency generation (DFG), covering more than 4.3 THz in telecom band, currently limited only by the accessible wavelength range of the our laser. By type-0 quasi-phase matched spontaneous parametric down conversion (SPDC), we generate correlated photon pairs in multiple spectral channels, each in a single fundamental spatial mode, and observe coincidence to accidental ratio (CAR) as high as 600, which is over an order of magnitude higher than in a lithium niobate microresonator with similar pump power [21].

2.   PPLN waveguide design and fabrication

The efficiency of parametric frequency conversions in PPLN nanowaveguides depends on the nonlinear susceptibility tensor, wave vector mismatch, spatial mode confinement and overlap of the interacting lights [5]. Taking those factors into account, in the undepleted pump approximation, the normalized conversion efficiency for SHG given as,

$$\eta = \frac{8\pi^2}{\epsilon_0 c \lambda_{2\omega}^2} \frac{d_{eff}^2}{n_{eff}^{2\omega}(n_{eff}^{\omega})^2} \frac{\iint E_{2\omega}^* E_\omega^2 \, dx \, dz}{\sqrt{\iint |E_{2\omega}|^2 \, dx \, dz \, \iint |E_\omega|^2 \, dx \, dz}} L^2 sinc^2(\Delta KL/2), \qquad (1)$$

where c is the speed of light in vacuum, ϵ_0 is the vacuum permittivity, d_{eff} is the effective nonlinear coefficient equal $\frac{2}{\pi} d_{33}$ in our case, ΔK is the wave vector mismatch, L is interaction length, $n_{eff}^{(\omega,2\omega)}$ and $E_{(\omega,2\omega)}(x,z)$ are the effective indices and electric fields of 1550-nm quasi-TE$_{00}$ and 775-nm quasi-TE$_{00}$ modes, respectively. We design the waveguide's cross-sectional geometry to realize strongly confined yet optimally overlapping fundamental spatial modes for all interacting lights, as permitted by poling. Specifically, we perform simulations (Lumerical MODE solution) to determine its ideal width and height for subwavelength mode confinement and over 90% overlap. These are crucial in ensuring high nonlinear efficiency while eliminating cross-mode interaction [14,22], which may prove necessary for achieving single photon nonlinearities in the future [23]. Besides, the use of fundamental spatial modes makes it easy for interfacing the current nanophotonic chips with other devices, such as coupling the single photon from the chips to single mode fibers (SMFs) for long distance quantum state transferring. In contrast, coupling higher order modes into a SMF is rather inefficient.

Furthermore, we periodically pole the waveguide to realize type-0 quasi-phase matching (QPM), with each interacting light guided in a TE mode to fully utilize the largest nonlinearity tensor d_{33} available on the X-cut LN thin film. For SHG, the QPM condition reads

$$\Delta K = k_{s,\,shg} - 2k_{p,\,shg} - \frac{2\pi}{\Lambda_{shg}} = 0, \qquad (2)$$

with $2\omega_{p,\,shg} = \omega_{s,\,shg}$. For SPDC, it reads

$$\Delta K = k_{p,\,spdc} - k_{s,\,spdc} - k_{i,\,spdc} - \frac{2\pi}{\Lambda_{spdc}} = 0, \tag{3}$$

with $\omega_{p,\,spdc} = \omega_{s,\,spdc} + \omega_{i,\,spdc}$. Here, $k_{j,\,l} = n_{eff}(\omega_{j,\,l},\ T)\omega_{j,\,l}/c$ is the wavenumber for the j-th lightwave, with $j = p,\ s,\ i$ corresponding to the pump, signal, and idler for SHG and SPDC processes. n_{eff} and $\omega_{j,\,l}$ are effective refractive index and angular optical frequency, respectively. T and Λ are the temperature and poling period of the PPLN. By using the temperature-dependent generalized Sellmeier equation and the Lumerical MODE solution to determine n_{eff} for interacting wavelengths in a mode matched nanowaveguide [14], we find that $k_{s,\,spdc} + k_{i,\,spdc} \approx 2k_{p,\,shg}$, over a wide bandwidth in telecom wavelengths (1500- 1600 nm). This implies $k_{s,\,shg} = k_{p,\,spdc}$ given that $\Lambda_{shg} = \Lambda_{spdc}$, allowing us to determine the optimum pump wavelength for SPDC by the means of identifying optimum second harmonic wavelength. Unlike the large period ($\Lambda > 10\mu m$) in traditional PPLN waveguides with weakly confined mode, the required poling period for tightly confined modes in LN nanowavguides will be very small ($\Lambda \sim 4\mu m$) due to much larger wavevector mismatch in Δk [5], posing a considerable challenge on the poling process. For this reason, the limitation on poling period is taken into consideration for the optimization of waveguide cross sectional geometries.

Figure 1(a) shows the optimized cross section of a LN nanowaveguide, with 500 nm in height, 1850 nm in the top width, and a 67° sidewall angle. The inclusion of the sidewall angle in our simulation is important for accurately simulating the optical modes to calculate the phase matching curve of the PPLN nanowaveguide. The required poling period for this geometry is about 4 μm. Figure 1(b) and (c) show the simulated profiles for the quasi-TE$_{00}$ modes at 775 nm and 1550-nm, respectively. The measured profile images are shown in Fig. 1(d) and (e), captured by using a high NA (0.45) aspheric lens with CMOS and IR cameras, respectively. As seen, these two modes are nearly identical, giving the excellent overlap of the interacting waves, as it is crucial to achieve efficient frequency conversion. Furthermore, the fundamental spatial mode over broad wavelength as seen in Fig. 1(d) and (e) can be very useful for coupling emission from quantum emitter [24] into PPLN for subsequent frequency conversion [25]. The use of such optimized spatial modes may prove crucial in extending the existing quantum technology to the challenging mid-IR regime [26,27]. According to Eq.(1), we firstly simulate the 775 and 1550 nm quasi-TE$_{00}$ modes via MODE solution. Then we extract the mode distributions, integrate and normalize them over the waveguide area. Last, we plug in constants (here $d_{33} \sim 27$ pm/V) and calculate, η_{norm} to be over $5,000\% W^{-1} cm^{-2}$. By further light confinement, even higher η_{norm} is possible [28,29], albeit requiring very short poling period (< 3 μm). This ultra-short period will be challenging to maintain high quality over a centimeter length. Nonetheless, recent progress on Z-cut LNOI could be a promising alternative approach for achieving uniform ultra-short poling period over such long length [30].

The PPLN waveguides are fabricated on an X-cut LNOI wafer (NANOLN Inc.), which is a 500 nm thick LN thin film bonded on a 2-μm thermally grown silicon dioxide layer above a silicon substrate, shown in Fig. 2(a). We use bi-layer electron-beam resist (495 PMMA A4 and 950 PMMA A4) and define the comb-shaped electrodes by using electron-beam lithography (EBL, Elionix ELS-G100, 100 keV). Then 15-nm Cr and 60-nm Au layers are deposited via electron-beam evaporation (AJA e-beam evaporator). The desirable poling electrode pattern is then created by a metal lift-off process. We apply several 450-V electric pulses, with 5-ms rising time, 20-ms flat-top and 10-ms decay time, on the poling pads, shown in Fig. 2(c), to form the domain inversion region shown in the dark color. Then a second EBL is carried out to define the LN waveguide in the poled region. Using a similar process described in our previous work [14], an optimized ion milling process is used to etch the waveguide structure with smooth sidewalls and the optimum sidewall angle. As shown in Fig. 2(e), we obtain uniform periodic
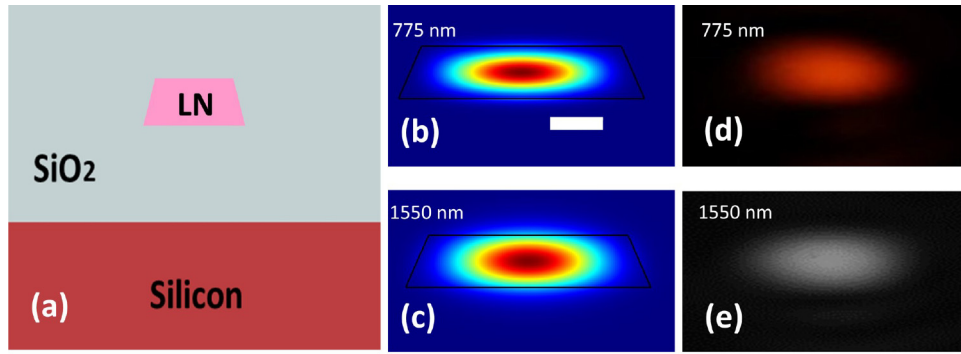
Fig. 1. (a) The cross-section of a typical PPLN nanowaveguide. (b)-(c) and (d)-(e) are the simulated and measured mode profiles for 775 nm and 1550 nm quasi-TE$_{00}$ mode, respectively. The scale bar is 500 nm.

domain inversion, which is crucial for high conversion efficiency. RCA ((5:1:1, deionized water, ammonia and hydrogen peroxide) bath for the removal of the redeposition is applied delicately to minimize the sidewall roughness due to the uneven removal rates for poled and unpoled regions. Later on, we clad the chip with 2 μm silicon oxide via Plasma-enhanced chemical vapor deposition (PECVD). The propagation loss of the PPLN waveguide is estimated to be 0.3dB/cm (see the Appendix A for more details).
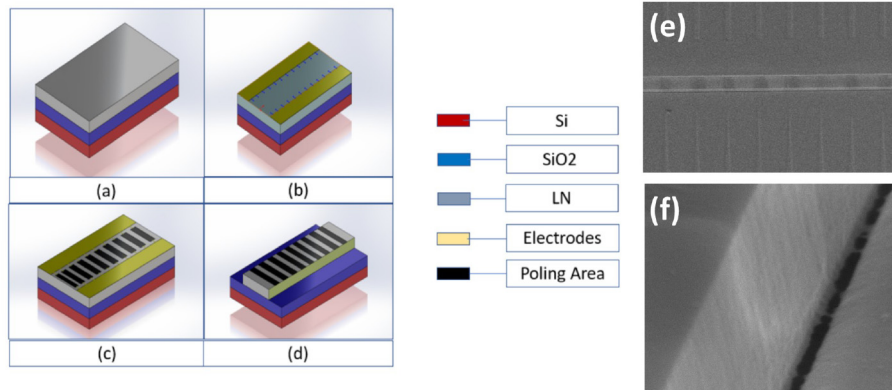

Fig. 2. (a) X-cut LNOI wafer. (b) Cr-AU Comb electrodes on LN wafer (c) Poling areas after several 20-ms high voltage pulses. (d) PPLN nanowaveguide after the complete fabrication process. Top silicon oxide cladding is not shown in (d). SEM images showing the (e) top view and (f) sidewall of PPLN waveguide before PECVD cladding.

With a smaller poling period, the acute field spreading effect between adjacent teeth become more significant, causing inconsistent domain wall profile. Therefore, in order to maintain the poling quality and acceptable yield for a small poling period ($\sim 4\mu m$), we use triangle-shape teeth on one side of the electrode while the other side remains in a rectangular shape for grounding. This helps form singly concentrated electrical fields for poling along the teeth direction toward the rectangular electrodes [31]. This minimizes the lateral spreading of the electric field and improves the poling quality considerably.

3. Nonlinear process in nanophotonic PPLN waveguides

3.1. Second harmonic and difference frequency generations

The experimental setup for the SHG efficiency measurement is similar as described in our previous work [28]. A continuous-wave (CW) tunable laser (Santec 550, 1500-1630 nm) is used as pump laser along with a fiber polarization controller to excite the fundamental quasi-TE mode in the PPLN waveguide. Two tapered fibers (2 μm spot diameter, OZ optics) serve as the input and output with losses of 4.3 dB per facet at 1550 nm and 5.4 dB per facet at 775 nm, respectively. Figure 3(a) shows the measured phase matching curve in the PPLN waveguide at T = 34.3 °C. The fitting envelope agrees well with the normalized theoretical phase matching curve indicating decent poling quality and well-satisfied quasi-phase matching. After taking the coupling loss into account, the measured on-chip pump power and SH power are 2.95 mW and 31.56 μW, respectively. This corresponding to normalized SHG efficiency for this PPLN waveguide with 4 mm length and 4 μm period of over $2200\%W^{-1}cm^{-2}$. We believe that lower measured normalized SHG efficiency compared to the theoretical prediction is primarily due to tolerances in device fabrication and poling process. Further improvement on poling process is possible by adding insulation layer such as silicon oxide to prevent current leakage [32] hence better poling uniformity. The oscillatory measured phase matching curve in Fig. 3(a) is caused by the Fabry-Perot (FP) cavity formed between the two polished facets on both end of the waveguide, which can be suppressed by having anti-reflection coating on both facets. Nonetheless, a well defined FP cavity is a noteworthy feature that can be used for preparing high dimensional quantum states [33]. Combining highly efficient SHG and light guiding in fundamental spatial mode over extended electromagnetic spectrum may unlock the potential toward chip-scale optical counting or atomic clocks on LN chip, as such, by harnessing its $\chi^{(2)}$ and $\chi^{(3)}$ nonlinearity for octave-spanning supercontinuum generation [34] and efficient coupling to atomic clocks [35].
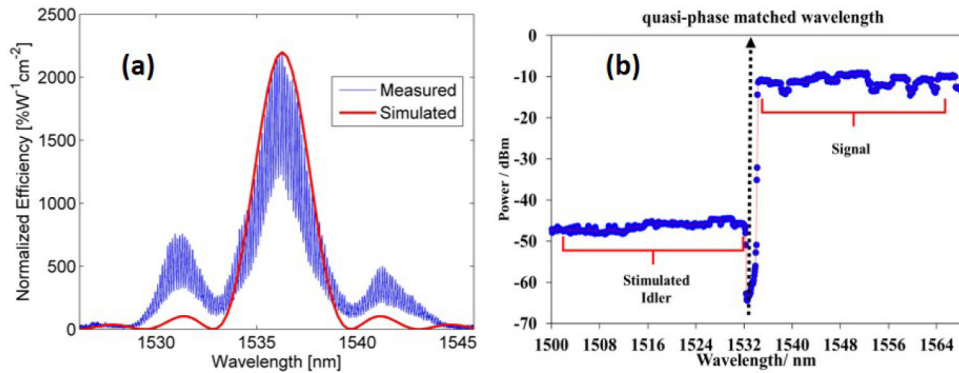

Fig. 3. (a) Phase match curve of PPLN waveguide. (b) DFG spectrum when pump at the phase-matched wavelength around 766.5 nm at 0.1 mW peak power in the waveguide. The discrepancy in center wavelength between (a) and (b) is mainly due to different coupling scheme.

Then, we characterize the phase matching bandwidth for difference frequency generation (DFG) by using the same PPLN waveguide. In this experiment, the pump and the signal are seeded from optical path 1 and 2 labeled in Fig. 4, respectively. The pump source is a CW tunable laser (Newport TLB-6712). Then, we fix the pumping wavelength while continuously sweep the signal wavelength (Santec 550) and record the generated idler power spectrum after the long pass filter (LPF) using an optical spectrum analyzer (not shown in Fig. 4). The pump wavelength (766.5 nm) in free-space coupled waveguide is slightly off from our previous center wavelength (768 nm) in lens-fiber coupled case due to highly mode size dependent phase matching condition

in nanowaveguide [14]. As shown in Fig. 3(b), a broadband DFG response (> 4.3 THz) is observed, only limited by the accessible laser wavelength. Figure 4, presents the recorded spectra in the telecom band. We observe average conversion rate of about - 37 dB with about $100 \mu W$ of on-chip pump power, comparable to cavity enhanced parametric generation on LN thin film [36]. The observed broadband DFG measurement promises generating multichannel correlated photon pairs or broadband on-chip parametric amplification with such PPLN nanowaveguides [37].
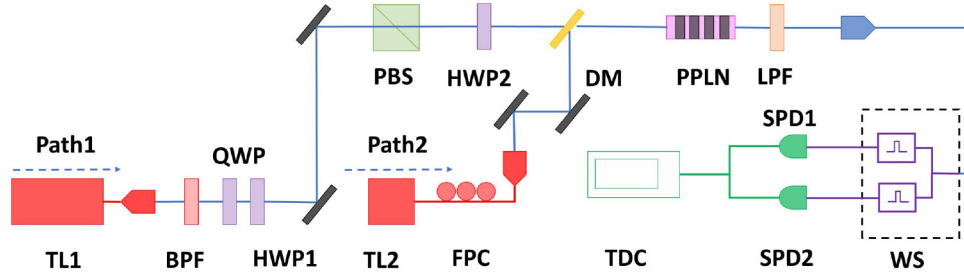

Fig. 4. Schematic of the experimental setup. The pump laser for photon pair generation is obtained from a visible tunable laser (TL1). The pump laser for SHG measurement is a near-infra-red tunable laser (TL2). BPF, band-pass filter, QWP, quarter-wave plate, HWP, half-wave plate, PBS, polarization beam splitter, DM, dichroic mirror, LPF, long-pass filter, SPD, single photon detector, WS, waveshaper, TDC, time-to-digital converter, FPC, fiber polarization controller.

3.2. Spontaneous parametric down-conversion

Next we examine the performance of this PPLN nanowaveguide for photon pair generation via SPDC. The experimental setup is shown in Fig. 4. In this experiment, the pump is a CW narrow linewidth (<200 KHz) tunable laser around 767 nm (Newport TLB-6712). It is collimated via a fiber collimator and guided through a half-wave plate, a quarter-wave plate and a polarization beam splitter to excite the quasi-TE mode in the waveguide. Then, an additional half-wave plate is used to fine tune the polarization angle prior to coupling into the LN chip by using an AR-coating aspheric lens. The temperature of the PPLN chip is stabilized at 34.3 $^{\circ}C$ by a heater with stability of 0.1 $^{\circ}C$. Subsequently, the generated photon pairs will be coupled out from the LN chip by using a second AR-coating aspheric lens. After rejecting the pump with a long-pass filter, the generated photon pairs in the telecom band will be collected into to a SMF-28 optical fiber with 70% coupling efficiency, achievable thanks to the well-defined fundamental spatial mode of the nanowaveguide. Such single-mode photons are vital for interfacing and manipulation of disparate quantum systems via photon-spin [38] and photon-quantum dot [39] interfaces. Then the signal and idler photons are separated by two 200 GHz bandpass filters (each over 35 dB extinction ratio) formed by a programmable WaveShaper (FINISAR). The photon pairs are detected by two synchronized, gated InGaAs single photon detectors with 100 MHz repetition rate and 1 ns gate width, detection efficiency of 5 % and dark count probability of 10^{-5}, where the coincidence counting events are recorded by using a time-to-digital converter [26].

To characterize the correlated photon pairs, we measure the single photon counts, coincidence counts, and accidental-coincidence counts as a function of the pump power to obtain the coincidence-to-accidental-counts ratio (CAR) [26]. The on-chip pump power is from 100 μW to 1 mW. The measured coincidence and accidental-coincidence at a different photon pair production rate is shown in Fig. 5(a). One can see that the coincidence rate increases linearly with photon production rate while the accidental-coincidence rate increases quadratically. This is because a coincidence event is a result of spontaneous down conversion where one pump photon is annihilated and two daughter (signal and idler) photons are created, as governed by energy

conservation in Eq. 3. Contrarily, the accidental-coincidence counts arise from the coincidence events of uncorrelated photons as a consequence of multiple photon pairs generation, especially with high pump power. We observe a CAR value of 631 ± 210 at photon production rate of 0.8 million pairs per second ($\approx 4{,}000$ pairs detected per second, considering 5% detection efficiency, 12 dB overall coupling loss and 10% pump peak power due to CW operation), corresponding to a brightness of 69 MHz/mW/nm. Note that the CAR value can be improved significantly by reducing the time-frequency detection modes by the means of narrow spectral filtering, time-gating, or the mode selective detection [40].
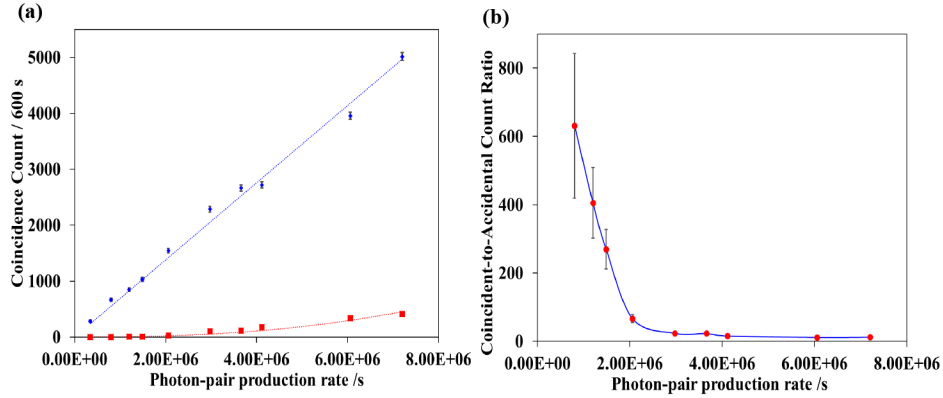
Fig. 5. (a) Measured coincidence (blue dots) and accidental (red squares) counts and (b) coincidence-to-accidental-counts ratio, CAR (red dot), as a function of photon production rate.

We characterize the spectral correlations between nine combinations of the signal and idler wavelength channels, as allowed by the total bandwidth of our programmable waveshaper as a tunable spectral filter (25 GHz). Here, we observe strong frequency correlations, where consistent photon coincidences were measured only for particular signal-idler combination as shown Fig. 6, where the diagonal coincidences spectra distribution reflects the energy and momentum conversations in the SPDC process. Nevertheless, the strong frequency correlation is anticipated to extend over a broad wavelength range as predicted by the observed DFG bandwidth [41], as shown in Fig. 3(b). Enabled by broadband and high purity correlated photon pairs generated on-chip, a potential quantum information application is near-deterministic generation of single photons via spectral multiplexing of heralded single-photon sources [42]. Furthermore, high purity correlated photon source can operate as a stable and accurate central synchronization clock source for deployment of distant interconnected quantum photonics chips within a quantum network [43–45].
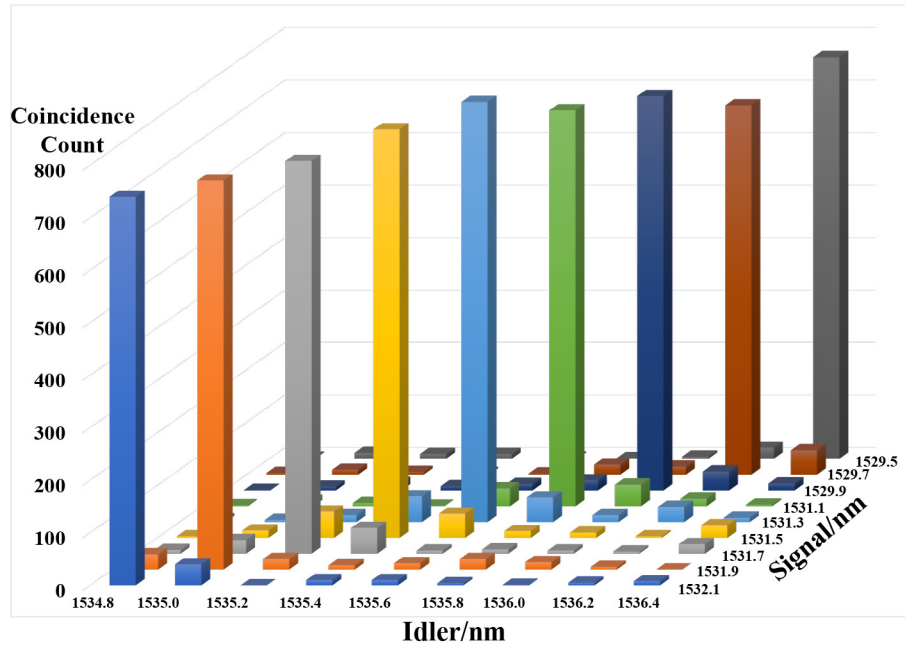
Fig. 6. Coincidence count measured at selected signal/idler wavelength combinations. Significant coincidence counts (corresponding to a peak) are observed only between channels fulfilling energy and momentum conservation.

4. Conclusion

In summary, we have realized a series of efficient parametric frequency conversions in an optimally mode-matched, periodic-poled lithium niobate nanowaveguide on chip. We first observed second harmonic generation and broadband difference frequency generation over 4.3 THz, whose normalized conversion efficiency is as high as 2200% $W^{-1}cm^{-2}$, thanks to the tight fundamental mode confinement for all interacting modes and high quality poling. Using the same PPLN nanowaveguide, we implemented a bright, wavelength multiplexing source of correlated photon pairs via spontaneous parametric down conversion, achieving coincidental-to-accidental ratios as high as 600 with only moderate spectral filtering. Highly efficient, optimally fundamental-mode matched and dense integrable, the present frequency conversion devices may find many applications in scalable nonlinear applications in both classical and quantum domains. The next steps will involve incorporating other optical elements on the same lithium-niobate chip, such as electro-optical modulation [46] wavelength multiplexing, to realize functional chips.

Appendix A:Loss measurement

In this section, we perform a comparison of the propagation loss between LN waveguide and PPLN waveguide. First, we fabricate microring resonators with similar dimension on the same type of LNOI wafer and used the same fabrication process. The highest intrinsic Q $\sim 2 \times 10^6$ (see Fig. 7(a)) is achieved on a 80 μm radius microring with 2 μm width. It is indicating the propagation loss is about 0.15 dB/cm. Second, to evaluate the propagation loss in PPLN waveguide, we apply standard Fabry-Perot method for estimation. As shown in Fig. 7(b), the loss is fitted to be 0.3 dB/cm. We could expect a slight degradation of the loss in the poled waveguide due to some extra roughness induced by wet cleaning process. This issue could be addressed

by reversing the fabrication step, i.e. carry out the poling step after the formation of the LN waveguide.
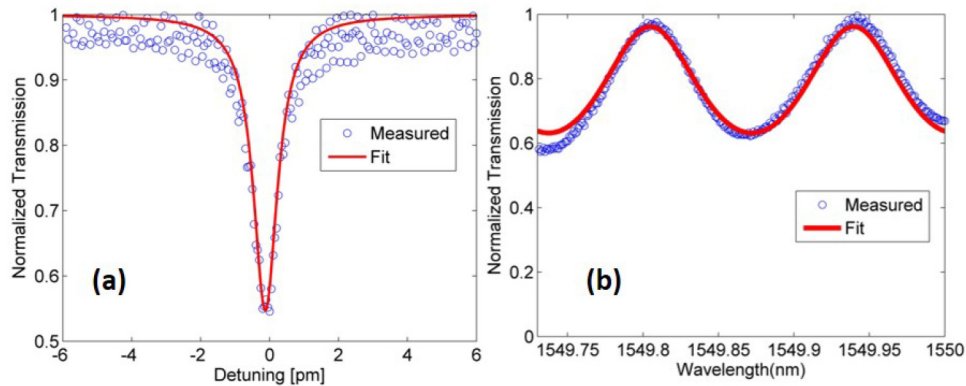
Fig. 7. (a) The spectrum of one mode which yields 2×10^6 quality factor at around 1600 nm. (b) The spectra of Fabry-Perot resonances formed by the PPLN wavguide and its two facets.

Acknowledgments

This fabrication was performed in part at the Advanced Science Research Center Nanofabrication Facility of the Graduate Center at the City University of New York.

References

1. F. Lenzini, J. Janousek, O. Thearle, M. Villa, B. Haylock, S. Kasture, L. Cui, H.-P. Phan, D. V. Dao, H. Yonezawa, P. K. Lam, E. H. Huntington, and M. Lobino, "Integrated photonic platform for quantum information with continuous variables," Sci. Adv. **4**(12), eaat9331 (2018).
2. L. Sansoni, K. H. Luo, C. Eigner, R. Ricken, V. Quiring, H. Herrmann, and C. Silberhorn, "A two-channel, spectrally degenerate polarization entangled source on chip," npj Quantum Inf. **3**(1), 5 (2017).
3. H. Chen, S. Auchter, M. Prilmüller, A. Schlager, T. Kauten, K. Laiho, B. Pressl, H. Suchomel, M. Kamp, S. Höfling, C. Schneider, and G. Weihs, "Time-bin entangled photon pairs from bragg-reflection waveguides," APL Photonics **3**(8), 080804 (2018).
4. H. Vahlbruch, M. Mehmet, K. Danzmann, and R. Schnabel, "Detection of 15 db squeezed states of light and their application for the absolute calibration of photoelectric quantum efficiency," Phys. Rev. Lett. **117**(11), 110801 (2016).
5. K. R. Parameswaran, R. K. Route, J. R. Kurz, R. V. Roussev, M. M. Fejer, and M. Fujimura, "Highly efficient second-harmonic generation in buried waveguides formed by annealed and reverse proton exchange in periodically poled lithium niobate," Opt. Lett. **27**(3), 179–181 (2002).
6. P. Rabiei, J. Ma, S. Khan, J. Chiles, and S. Fathpour, "Heterogeneous lithium niobate photonics on silicon substrates," Opt. Express **21**(21), 25573–25581 (2013).
7. A. Rao, M. Malinowski, A. Honardoost, J. R. Talukder, P. Rabiei, P. Delfyett, and S. Fathpour, "Second-harmonic generation in periodically-poled thin film lithium niobate wafer-bonded on silicon," Opt. Express **24**(26), 29941–29947 (2016).
8. L. Chang, Y. Li, N. Volet, L. Wang, J. Peters, and J. E. Bowers, "Thin film wavelength converters for photonic integrated circuits," Optica **3**(5), 531–535 (2016).
9. A. Boes, L. Chang, M. Knoerzer, T. G. Nguyen, J. D. Peters, J. E. Bowers, and A. Mitchell, "Improved second harmonic performance in periodically poled lnoi waveguides through engineering of lateral leakage," arXiv preprint arXiv:1906.02383 (2019).
10. C. Wang, M. Zhang, X. Chen, M. Bertrand, A. Shams-Ansari, S. Chandrasekhar, P. Winzer, and M. Loncar, "Integrated lithium niobate electro-optic modulators operating at cmos-compatible voltages," Nature **562**(7725), 101–104 (2018).

11. C. Wang, C. Langrock, A. Marandi, M. Jankowski, M. Zhang, B. Desiatov, M. M. Fejer, and M. Lončar, "Ultrahigh-efficiency wavelength conversion in nanophotonic periodically poled lithium niobate waveguides," Optica **5**(11), 1438–1441 (2018).

12. L.-H. Hong, B.-Q. Chen, C.-Y. Hu, and Z.-Y. Li, "Analytical solution of second-harmonic generation in a lithium-niobate-birefringence thin-film waveguide via modal phase matching," Phys. Rev. A **98**(2), 023820 (2018).

13. J.-Y. Chen, Y. M. Sua, Z.-T. Zhao, M. Li, and Y.-P. Huang, "Observation of quantum zeno blockade on chip," Sci. Rep. **7**(1), 14831 (2017).

14. J.-Y. Chen, Y. M. Sua, H. Fan, and Y.-P. Huang, "Modal phase matched lithium niobate nanocircuits for integrated nonlinear photonics," OSA Continuum **1**(1), 229–242 (2018).

15. R. Luo, Y. He, H. Liang, M. Li, and Q. Lin, "Semi-nonlinear nanophotonic waveguides for highly efficient second-harmonic generation," Laser Photonics Rev. **13**(3), 1800288 (2019).

16. A. Sipahigil, R. E. Evans, D. D. Sukachev, M. J. Burek, J. Borregaard, M. K. Bhaskar, C. T. Nguyen, J. L. Pacheco, H. A. Atikian, C. Meuwly, R. M. Camacho, F. Jelezko, E. Bielejec, H. Park, M. Lončar, and M. D. Lukin, "An integrated diamond nanophotonics platform for quantum-optical networks," Science **354**(6314), 847–850 (2016).

17. S. Aghaeimeibodi, B. Desiatov, J.-H. Kim, C.-M. Lee, M. A. Buyukkaya, A. Karasahin, C. J. K. Richardson, R. P. Leavitt, M. Loncar, and E. Waks, "Integration of quantum dots with lithium niobate photonics," Appl. Phys. Lett. **113**(22), 221102 (2018).

18. S. Wehner, D. Elkouss, and R. Hanson, "Quantum internet: A vision for the road ahead," Science **362**(6412), eaam9288 (2018).

19. F. Kaiser, P. Vergyris, A. Martin, D. Aktas, O. Alibart, and S. Tanzilli, "Quantum optical frequency conversion for polarisation entangled qubits: towards interconnected quantum information devices," arXiv e-prints arXiv:1901.09826 (2019).

20. X. Lu, Q. Li, D. A. Westly, G. Moille, A. Singh, and V. Anant, "Chip-integrated visible-telecom photon pair sources for quantum communication," arXiv e-prints arXiv:1805.04011 (2018).

21. R. Luo, H. Jiang, S. Rogers, H. Liang, Y. He, and Q. Lin, "On-chip second-harmonic generation and broadband parametric down-conversion in a lithium niobate microresonator," Opt. Express **25**(20), 24531–24539 (2017).

22. R. Luo, Y. He, H. Liang, M. Li, and Q. Lin, "Highly tunable efficient second-harmonic generation in a lithium niobate nanophotonic waveguide," Optica **5**(8), 1006–1011 (2018).

23. T. Guerreiro, A. Martin, B. Sanguinetti, J. S. Pelc, C. Langrock, M. M. Fejer, N. Gisin, H. Zbinden, N. Sangouard, and R. T. Thew, "Nonlinear interaction between single photons," Phys. Rev. Lett. **113**(17), 173601 (2014).

24. S. L. Mouradian and D. Englund, "A tunable waveguide-coupled cavity design for scalable interfaces to solid-state quantum emitters," APL Photonics **2**(4), 046103 (2017).

25. S. Zaske, A. Lenhard, C. A. Keßler, J. Kettler, C. Hepp, C. Arend, R. Albrecht, W.-M. Schulz, M. Jetter, P. Michler, and C. Becher, "Visible-to-telecom quantum frequency conversion of light from a single quantum emitter," Phys. Rev. Lett. **109**(14), 147404 (2012).

26. Y. M. Sua, H. Fan, A. Shahverdi, J.-Y. Chen, and Y.-P. Huang, "Direct generation and detection of quantum correlated photons with 3.2 um wavelength spacing," Sci. Rep. **7**(1), 17494 (2017).

27. D. A. Kalashnikov, A. V. Paterova, S. P. Kulik, and L. A. Krivitsky, "Infrared spectroscopy with visible light," Nat. Photonics **10**(2), 98–101 (2016).

28. J.-Y. Chen, Y. M. Sua, Z. Ma, C. Tang, Z. Li, and Y.-P. Huang, "Efficient second-harmonic generation in sub-micron ppln waveguides," in *Frontiers in Optics / Laser Science* (Optical Society of America, 2018), p. JTu2A.87.

29. S. Fathpour, "Heterogeneous nonlinear integrated photonics," IEEE J. Quantum Electron. **54**(6), 1–16 (2018).

30. T. R. Volk, R. V. Gainutdinov, and H. H. Zhang, "Domain-wall conduction in afm-written domain patterns in ion-sliced linbo3 films," Appl. Phys. Lett. **110**(13), 132905 (2017).

31. M. Reich, F. Korte, C. Fallnich, H. Welling, and A. Tünnermann, "Electrode geometries for periodic poling of ferroelectric materials," Opt. Lett. **23**(23), 1817–1819 (1998).

32. J. T. Nagy and R. M. Reano, "Periodic poling of ion-sliced x-cut magnesium oxide doped lithium niobate thin films," in *Conference on Lasers and Electro-Optics*, (Optical Society of America, 2018), p. SF2I.2.

33. C. Autebert, A. Minneci, G. Maltese, J. Belhassen, A. Lemaître, M. Amanti, F. Baboux, T. Coudreau, P. Milman, and S. Ducci, "On-chip generation of frequency-entangled qudits," in *Quantum Information and Measurement (QIM) 2017* (Optical Society of America, 2017), p. QW2C.2.

34. M. Yu, B. Desiatov, Y. Okawachi, A. L. Gaeta, and M. Loncar, "Coherent two-octave-spanning supercontinuum generation in lithium-niobate waveguides," arXiv e-prints arXiv:1901.11101 (2019).

35. D. R. Carlson, D. D. Hickstein, A. Lind, J. B. Olson, R. W. Fox, R. C. Brown, A. D. Ludlow, Q. Li, D. Westly, H. Leopardi, T. M. Fortier, K. Srinivasan, S. A. Diddams, and S. B. Papp, "Photonic-chip supercontinuum with tailored spectra for counting optical frequencies," Phys. Rev. Appl. **8**(1), 014027 (2017).

36. R. Luo, Y. He, H. Liang, M. Li, J. Ling, and Q. Lin, "Optical parametric generation in a lithium niobate microring with modal phase matching," Phys. Rev. Appl. **11**(3), 034026 (2019).

37. Y. M. Sua, J.-Y. Chen, and Y.-P. Huang, "Ultra-wideband and high-gain parametric amplification in telecom wavelengths with an optimally mode-matched ppln waveguide," Opt. Lett. **43**(12), 2965–2968 (2018).

38. D. D. Awschalom, R. Hanson, J. Wrachtrup, and B. B. Zhou, "Quantum technologies with optically interfaced solid-state spins," Nat. Photonics **12**(9), 516–527 (2018).

39. U. Paudel, J. J. Wong, M. Goggin, P. Kwiat, A. S. Bracker, M. Yakes, D. Gammon, and D. Steel, "Direct Excitation of a Single Quantum Dot with Cavity-SPDC Photons," arXiv e-prints arXiv:1812.07165 (2018).

40. A. Shahverdi, Y. M. Sua, L. Tumeh, and Y.-P. Huang, "Quantum parametric mode sorting: Beating the time-frequency filtering," Sci. Rep. **7**(1), 6495 (2017).

41. M. Liscidini and J. E. Sipe, "Stimulated emission tomography," Phys. Rev. Lett. **111**(19), 193602 (2013).

42. M. Grimau Puigibert, G. H. Aguilar, Q. Zhou, F. Marsili, M. D. Shaw, V. B. Verma, S. W. Nam, D. Oblak, and W. Tittel, "Heralded single photons based on spectral multiplexing and feed-forward control," Phys. Rev. Lett. **119**(8), 083601 (2017).

43. A. Valencia, G. Scarcelli, and Y. Shih, "Distant clock synchronization using entangled photon pairs," Appl. Phys. Lett. **85**(13), 2655–2657 (2004).

44. C. Ho, A. Lamas-Linares, and C. Kurtsiefer, "Clock synchronization by remote detection of correlated photon pairs," New J. Phys. **11**(4), 045011 (2009).

45. E. O. Ilo-Okeke, L. Tessler, J. P. Dowling, and T. Byrnes, "Remote quantum clock synchronization without synchronized clocks," npj Quantum Inf. **4**(1), 40 (2018).

46. M. Jin, J.-Y. Chen, Y. M. Sua, and Y.-P. Huang, "High-extinction electro-optic modulation on lithium niobate thin film," Opt. Lett. **44**(5), 1265–1268 (2019).